Nanoscale

Accepted Manuscript

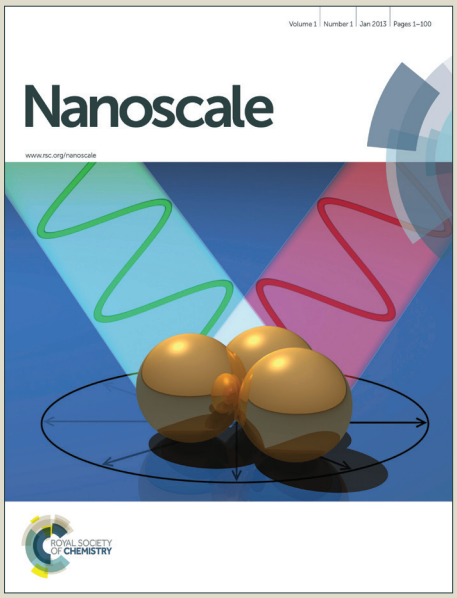

Journal Name Nanoscale Dynamic Article Links ►

Cite this: DOI: 10.1039/c0xx00000x

www.rsc.org/xxxxxx

ARTICLE TYPE

Multifunctional ScF_3: Ln^{3+} (Ln = Tb, Eu, Yb, Er, Tm and Ho) nano/microcrystals: hydrothermal/solvothermal synthesis, electronic structure, magnetism and tunable luminescence properties

Lili Han[a], Yuhua Wang[a]*, Linna Guo[a], Lei Zhao[a], Ye Tao[b]

Received (in XXX, XXX) Xth XXXXXXXXX 20XX, Accepted Xth XXXXXXXXX 20XX
DOI: 10.1039/b000000x

A facile hydrothermal/solvothermal route has been developed to synthesize a series of multifunctional lanthanide ions (Tb^{3+}, Eu^{3+}, Yb^{3+}, Tm^{3+}, Er^{3+} and Ho^{3+}) activated ScF_3 nanocrystals. The morphology and size of ScF_3 can be tuned in a controlled manner by altering the additives and volume ratios of H_2O:EtOH in the initial solution. Under ultraviolet (UV), vacuum ultraviolet (VUV) or low-voltage electron beam excitation, the as-obtained Tb^{3+}, Eu^{3+} codoped ScF_3 product exhibit multicolor photoluminescence (PL) and cathodoluminescence (CL) emissions and the possible luminescence mechanisms are discussed. Meanwhile, under 980 nm excitation, up-conversion (UC) emissions have been achieved in Yb^{3+}–Er^{3+}, Yb^{3+}–Tm^{3+}, and Yb^{3+}–Ho^{3+} codoped ScF_3, respectively. A ferromagnetic property of ScF_3 is detected due to the nanocrystal defects. All in all, the obtained results indicate that the lanthanide ions doped ScF_3 nanocrystals exhibit multicolor UV/VUV PL, CL, UC luminescence and ferromagnetism properties, which may find their potential applications for PL areas, field emission display devices and bioseparation and magnetic resonance imaging and so forth.

1. Introduction

In modern chemistry and materials, the optical, magnetic, and catalytic properties of the rare-earth elements including lanthanide (Ln^{3+}) series, scandium and yttrium remain fascinating, with applications ranging from optical, magnetic bio-imaging, lasers and catalysts in the petrochemical industry. Particularly, Ln^{3+}-doped phosphors with good optical properties have received considerable attention due to their application in fields such as light-emitting diodes (LEDs), field emission displays (FEDs), three-dimensional (3D) plasma display panels (PDPs), Hg-free lamps, biological assays and medical imaging involved in upconvertion (UC) phosphors[1-4]. Unfortunately, the phosphors applied in above devices have some fatal disadvantages and details are as follows. So far, the lack of proper red phosphor becomes the bottleneck for the blue or near-ultraviolet LED based white LEDs[5]. And many problems still remain for PDP phosphors, including poor color purity for the red phosphor, thermal and aging degradation for the blue phosphor, and long decay time for the green phosphor, which especially can't meet the requirement of 3D PDPs[6-9]. Most oxide-based phosphors explored recently such as Y_2SiO_5:Ce^{3+}, Sr_2CeO_4:Bi^{3+} have low electrical conductivity for FED devices[10-12]. And low efficiency strongly limits the practical application of UC phosphors. Based on these shortcomings, it is imperious to explore some new phosphors with high luminescent efficiency, wide band gap aiming to optical and pony size aiming to high resolution display or biological assays, and if possible, it would be better they contain a variety of functions.

Aiming at the lack of proper red phosphor for LEDs and PDPs, Eu^{3+}, with a red emission ascribed to the f–f electronic transition has attracted much attention. And for the display and lighting devices, an efficient manner for enhancing the luminescence efficiency is by sensitization[13-15]. Hereinto, the energy transfer (ET) from Tb^{3+} to Eu^{3+} was observed and various mechanisms were discussed depending on the different matrixes upon ultraviolet (UV) light[16, 17]. In addition to these, it has been reported that the vacuum ultraviolet (VUV) sensitization effect in Tb^{3+}-Eu^{3+} codoped systems paves the ways for the creation of efficient VUV phosphors[18-20]. Furthermore, the Ln^{3+} double doping even triple doping can achieve multicolor luminescence, which is very entertaining and practical for the fields of solid-state lighting and display.

Involved in host matrix for ET, fluoride is a kind of good host material compared with oxide, because it normally possesses low phonon energy. This leads to the low probability of non-radiative decay, and consequently the luminescence quantum yields are usually higher than in oxide hosts[21, 22]. So rare earth fluorides have the potential to the realization of efficient ET. At the present, Yb^{3+}, Er^{3+}/Tm^{3+}/Ho^{3+} doped fluorides nanocrystals have been explored as excellent UC luminescence materials applied for the biological assays and medical imaging, especially in recent years, single-band and white UC luminescence properties of these materials are attractive for anti-counterfeiting, color display applications, solid-state 3D displays and so on[23-31]. However, relatively few researchers pay attention to the ET from Tb^{3+} to Eu^{3+} in fluoridematrix. Up to now, great efforts have been made

on the synthesis of LnF_3 nanocrystals with promising applications above [32, 33]. The element Y is, strictly speaking, not a lanthanide, but on account of its very similar chemical properties, it is often expected as high accommodation of rare earth luminescent centers without adding charge compensators[34, 35]. Although Sc is in the same main group with Y, ScF_3, as another important host material has been rarely reported. ScF_3, belongs to the general molecular formula ABX_3. Commonly, this kind of structure includes three phase: cubic, rhombohedral and orthorhombic. Recently, K. S. Aleksandrov *et al* demonstrated that in the normal temperature and pressure conditions, cubic ScF_3 is the most stable[36]. ScF_3, as a novel fluoride matrix, is known to be with space group Pm-3m, Z = 1 and the transition is associated with the rotation of ScF_6 octahedra around the three fold axis[37]. In 2010, Benjamin K. Greve and co-workers demonstrated that cubic ScF_3 showed pronounced negative thermal expansion[38]. To the best of our knowledge, up to now, the fundamental physical and chemical properties of ScF_3 (for example, the electronic structure, controlled synthesis and optical properties) are not well understood. On the other hand, LnF_3 nano-material has many interesting properties and applications that differ from those of the bulk materials, such as biological labels, detection, and magnetic resonance imaging as mentioned above[39, 40]. As far as the synthesis techniques, the most popular ones for controllably preparing novel nano-and micro- structures involve hydrothermal and solvothermal synthesis routes[41, 42]. And materials which can meet the morphology-controlled synthesis are often the materials with simple structure and component. Therefore, ScF_3 can be very appropriate in structure.

Considering a foundational research on the properties and the multifunctional application, in this work, Tb^{3+}, Eu^{3+}, Yb^{3+}, Er^{3+}, Ho^{3+} and Tm^{3+} doped ScF_3 are taken as target materials to study. In addition to the morphology, crystal structure and electronic structure studies, the nanocrystal defects participant photoluminescence (PL) and cathodoluminescence (CL) as well as UC and the magnetism of properties of as-prepare samples are studied.

2. Experimental

2.1 Synthesis

Materials: The raw materials Sc_2O_3 (99.99%), NH_4F (99.9%), Eu_2O_3 (99.99%), Tb_4O_7 (99.99%), Yb_2O_3 (99.99%), Er_2O_3 (99.99%), Tm_2O_3 (99.99%), Ho_2O_3 (99.99%) were all purchased from Beijing non-ferrous metals research institute and used directly without further purification.

Synthesis process: ScF_3 nano- and micro-crystals were synthesized by a hydrothermal/solvothermal process. In a typical hydrothermal process, 1 m mol Sc_2O_3 was dissolved in dilute H_3NO_3 solution (1:1 v/v) by heating to 80 ℃ with agitation to form clear $Sc(NO_3)_3$ aqueous solution (labeled solution a). 0.1 g Citric acid trisodium salt dehydrate (Cit^{3-}), (or Ethylene diamine tetraacetic acid (EDTA), Hexadecyl trimethyl ammonium bromide (CTAB)) was added into 10 mL of deionized water under vigorous stirring until the additive was dissolved absolutely to form transparent solution (labeled solution b). Then solution b was added into solution a to form the solution c containing Sc-A complex (A=additive). Subsequently, 4 mL NH_4F (1 M) was added to the above aqueous solution c under vigorous stirring. The pH value of the mixed solution was adjusted to 1. After additional agitation for 1 h, the as-obtained mixed solution was transferred into a Teflon bottle held in a stainless steel autoclave, sealed and maintained at 180 ℃ for 24 h. The system was cooled to room-temperature naturally, and the product was collected, purified by ethanol and deionized water several times, and dried at 80 ℃ for 12 h. In a typical solvothermal process, most process was same with that of hydrothermal process, except for the difference that additive was added into 10 mL of mixture of H_2O and EtOH to form solution b. The Ln^{3+} doped ScF_3 nanocrystals were prepared by the same procedure, except for adding additional relevant Ln^{3+} (Ln = Eu, Tb, Yb, Er, Tm and Ho) into the solution of $Sc(NO_3)_3$ at the initial stage.

2.2 Characterization

The X-ray diffraction (XRD) patterns were obtained on Rigaku D/max-2400 powder diffractometer using Cu Kα radiation (1.5418) at 40 kV and 60 mA. The morphologies of the as-prepared samples were inspected by field emission scanning electron microscope (FESEM, Hitachi, S-4800), transmission electron microscopy (TEM) and highresolution transmission electron microscopy (HRTEM) (FEI Tecnai F30, operated at 300 kV). The selected area electron diffraction (SAED) and energy dispersive X-ray spectroscopy (EDX) were attached with the same TEM. Images were acquired digitally on a Gatan multipole CCD camera. The Fourier transform infrared spectroscopy (FTIR) spectra were measured with Nicolet NEXUS 670 infrared spectrophotometer with the KBr pellet technique. The UV PL and PL excitation (PLE) spectra were measured by FLS920T spectrophotometer equipped with VM504 vacuum monochromator using Deuterium/Xe lamp as light source, and the VUV luminescent spectra were measured at the VUV spectroscopy experimental station on beam line 3B1B, Beijing Synchrotron Radiation Facilities (BSRF). Low-voltage CL spectra were obtained using a modified Mp-Micro-S instrument. The UC emission spectra were recorded using the 980 nm Laser Diode (LD) as excitation source, with the HORIBA Jobin Yvon Fluorlog-3 Spectro fluorometer system. The measurement of magnetic property was using vibrating sample magnetometer (VSM) (Lakeshore 7304). All the measurements were performed at room temperature (RT).

3. Results and Discussion

3.1 X-ray diffraction patterns

The purity of all the prepared samples is checked by XRD. Figure 1 shows the typical XRD patterns of ScF_3, $Sc_{0.895}Yb_{0.1}Er_{0.005}F_3$ and $Sc_{0.89}Tb_{0.1}Eu_{0.01}F_3$ samples. By comparing with JCPDS Card No. 85-1078, which is also plotted in Fig. 1, all the observed peaks can be indexed to the pure phase of ScF_3. No phase transformation or impurity is observed. The diffraction peaks of $Sc_{0.89}Tb_{0.1}Eu_{0.01}F_3$ and $Sc_{0.895}Yb_{0.1}Er_{0.005}F_3$ samples are shifted a little to lower angles with respecting to the position of standard ScF_3. This is because the radius of Ln^{3+} (Ln = Tb, Eu, Yb, Er, Tm and Ho) are bigger than that of Sc^{3+} in the ScF_3 host lattice, indicating that Ln^{3+} have been effectively built into ScF_3 host lattice.

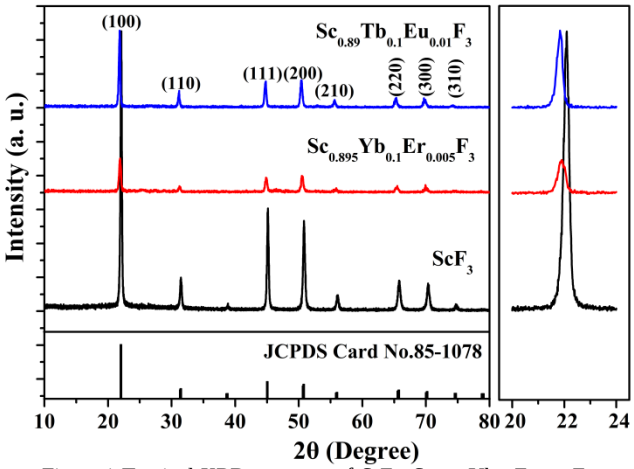

Figure 1 Typical XRD patterns of ScF_3, $Sc_{0.895}Yb_{0.1}Er_{0.005}F_3$ and $Sc_{0.89}Tb_{0.1}Eu_{0.01}F_3$ samples

3.2 Morphology and microstructure of the products

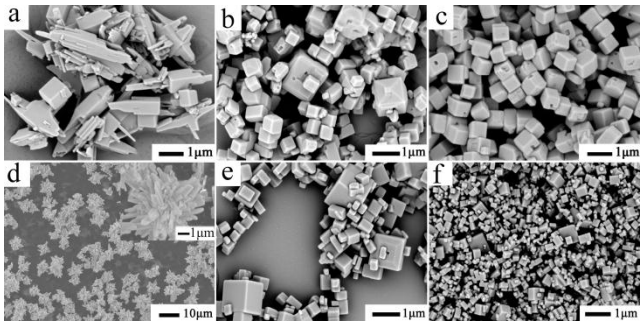

Fig. 2 SEM images of evolution for ScF_3 at different hydrothermal times without any additives: (a) 5.5h, (b) 12 h, (c) 24 h; SEM images of the ScF_3 prepared by hydrothermal process at 24h with different additives:(d) Cit^{3-}, (e) EDTA and (f) CTAB.

Fig. 2a–c depicts the SEM photographs of ScF_3 with various hydrothermal times. At the initial stage within 5.5 h, the product exhibits agglomerated littery microrods(1~2 um), and there are few cubic crystals at the same time. When the reactant undergoes hydrothermal treatment for 12 h, it can be seen from Fig. 2b that the cubic shapes on a different scale are dominated while the microrods are few. After 24 h, the reaction has been completed and monodisperse and uniform cubes with a side length of 500 nm are formed. Generally, in addition to the reaction time, different additives could influence the morphology, too. To study the effect of different additives on the morphology, sample with either Cit^{3-} (d) or EDTA (e) or CTAB (f) as additive is prepared. The typical SEM images of samples are given in Fig. 2d, e and f, respectively. Good dispersion and uniform acianthus shapes are obtained for sample with introducing Cit^{3-}. From the enlarged images of Fig. 2d, needles are observed to assemble into mono disperse cluster with an average length of 4 μm. From SEM image (Fig. 2e) of ScF_3 with EDTA as additive, a series of cubes are obtained. It is obvious that all the edges of cubes become incisive. In contrast, when CTAB is introduced, the size of cubes remarkably decreases to be below 200 nm and became more uniform. It is just because the solution of the CTAB contains hydrophobic C–N organic groups, which could chelate metal ions and hinder particle aggregation[43, 44]. The above results indicate that the additives have a remarkable different impact on the morphologies of the final products, which could be related to the differences of the chelating constant with Sc^{3+} [45-47]. Especially, CTAB plays arresting roles of dispersant and crystal growth oriented agent during the hydrothermal process.

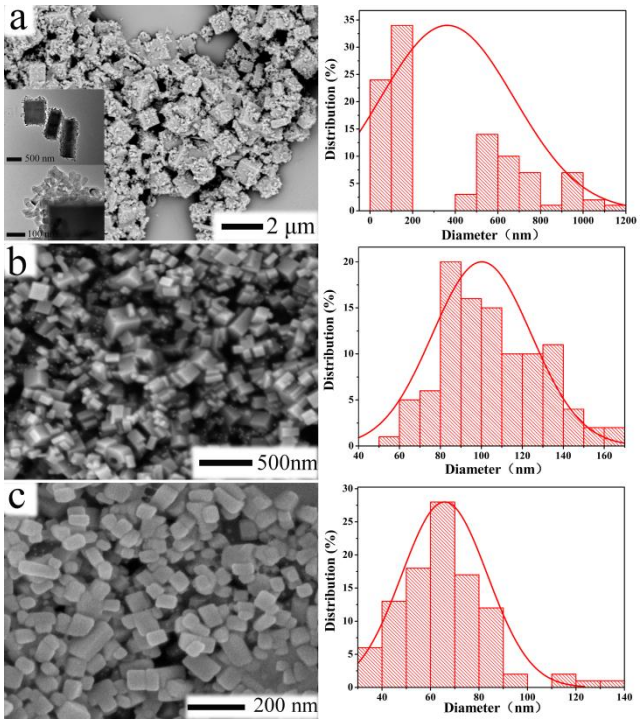

Fig. 3 SEM images (left) and size distributions (right) of ScF_3 nanoparticles with component solvent of different volume ratios of H_2O:EtOH: (a) 1:2, (b) 1.:4, (c) 1:6

Based on the above results, considering the influence of the solvent, we continue preparing a series of ScF_3 nano and micro particles with component solvent of different volume ratios of H_2O:EtOH by a CTAB participant solvothermal process. It turns out that the morphologies and sizes of the samples are tuned by varying the volume ratios of H_2O:EtOH from 1:2 to 1:6. As indicated in Fig. 3 by the SEM images (left) and grain size distributions (right, about 100 individual particle sizes are measured for each sample), it can be seen that with increasing EtOH content (Fig. 3a–c), the cubic particles' size grows smaller and their surface becomes smoother as a whole. In contrast with the EtOH free sample, component solvent with two times of EtOH leads to slightly larger particles with sizes about 500 nm (Fig. 3a). To examine the morphology characteristics further, TEM images are studied, as shown in the inset of Fig. 3a. Interestingly, the microparticles with unformed cubic shapes about 200 nm revolve around a central bid regular cube with a size of 500 nm, consistent with the result of SEM. It is worth noting that the size decreases more quickly when H_2O:EtOH volume ratio is 1:4, and the surface just looks completely smooth and integrated. Further increasing the EtOH content to 6 times, plenty of almost uniform and regular cubes with an average length of about 60 nm can be seen in Fig. 3c. No other morphologies can be observed, indicating a high yield of cubic nanostructures. It is evident from SEM images that the different morphologies can be obtained by solvothermal process with

different volume ratios of H_2O:EtOH. It can be due to the fact that the mixed solvent has different viscosity and different amount of EtOH molecules are capped on the ScF_3 nuclei, which can control the growth rate and direction of the product. Therefore, it can be concluded that EtOH could have double functions of structure-directing reagent and solvent in present case[48].

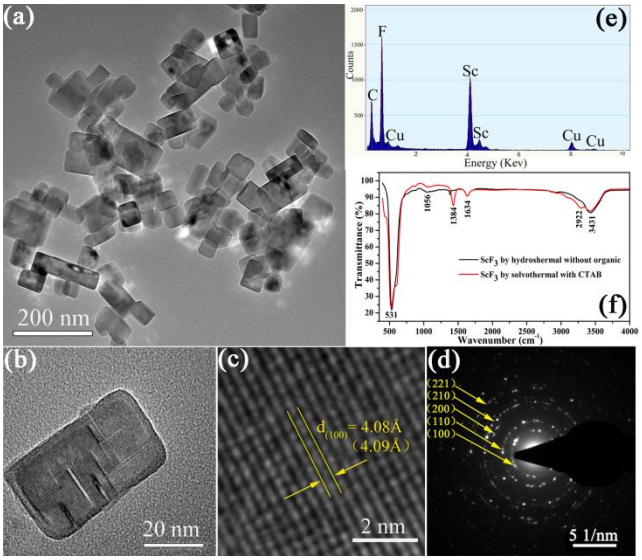

Fig. 4 Representative (a) large-scale TEM image, (b) single particle TEM image, (c) HRTEM image, (d) SAED pattern, (e) EDX spectrum (f) FT-IR spectra of ScF_3 by hydrothermal without any organic (blank line) and ScF_3 by solvothermal with CTAB (red line)

It is found that the particles have a nearly uniform cubic shape with a side length of 60 nm by solvothermal process with component solvent of ratios of H_2O:EtOH = 1:6 and are well dispersed when treated with CTAB within solvothermal time. The microstructure of the typical ScF_3 nanocubes is examined by TEM, HRTEM, SAED, EDX and FT-IR. Figure 4a shows the TEM image of the as-synthesized ScF_3 nanocubes. It can be observed that the nanocubes have quasi-cuboid-plate shape and the single nanocube given in Fig. 4b reveals some clear lattice fringes as well. The HRTEM of the ScF_3 nanocube present its highly crystalline nature as shown in Fig. 4c. The inter-planar distances of HRTEM are determined to be about 4.08 Å, corresponding to the (100) lattice plane of the cubic phase of ScF_3, which is consistent with the XRD analysis. SAED patterns in Fig. 4d show clear diffraction rings corresponding to the specific (100), (110), (200), (210) and (221) planes. SAED patterns confirm polycrystalline nature due to observation of diffraction rings. The EDX analysis spectrum of ScF_3 is given in Fig. 4e, which confirms the presence of Sc, F, C and Cu in the sample, and the Cu peak is ascribed to the copper grid supporting the TEM sample. FT-IR is employed as an additional probe to testify the presence groups of the ScF_3 by hydrothermal without any organic (blank line) and ScF_3 by solvothermal with CTAB (red line), as shown in Fig. 4f. An intense and broad band at 3400-2900 cm^{-1} is assigned to the O–H stretching vibrations of scandium hydroxide. The band at 1633 and 1384 cm^{-1} can be both attributed to the C–O vibration from the organics on the sample surface. These C–O vibrations can root in the residuary EtOH after the purified process. It can also be seen that the strongest band around 531 cm^{-1} is assigned to the vibration of the ScF_3 compound. The intensities of above bands of the ScF_3 by solvothermal with CTAB are similar except the band at 1384 cm^{-1} due to the increasing of the organic matter. In the next section, all the properties including electronic structure, luminescence and magnetism are taken from the samples prepared via solvothermal reaction used CTAB as the additive and the mixed solvent with H_2O:EtOH volume ratios of 1:6 within 24h solvothermal time.

3.3 Band structures and density of states

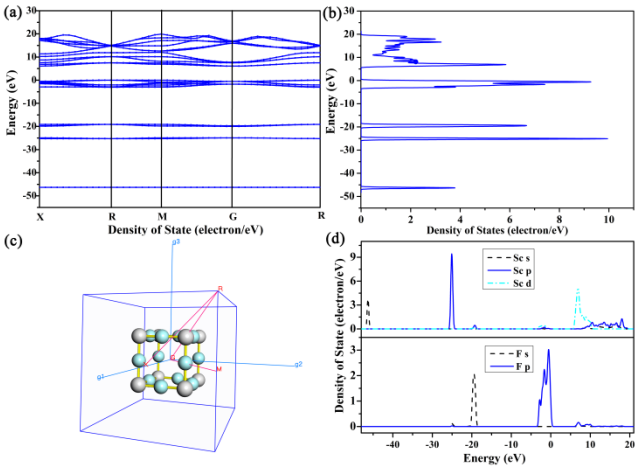

Fig. 5 (a) Band structure, (b) density of states, (c) Brillouin zone, (d) partial density of states.

The density functional theory calculations of ScF_3 are shown in Fig. 5. The local density approximation (LDA) is chosen for the theoretical basis of the density function. ScF_3 possesses an indirect band gap of about 6.075 eV with the valence band (VB) maximum at the X point and the conduction band (CB) minimum at the R point of the Brillouin zone. The electronic structure of the VB originates predominantly from F 2p states, whereas the CB is composed mostly of Sc 3d states. These calculation results demonstrate that ScF_3 provides a broad band gap to contain the energy levels of Ln^{3+}, which makes Ln^{3+} be suitable for acting as the emission center.

3.4 luminescence properties

3.4.1 Sensitization of Tb^{3+} to Eu^{3+} in ScF_3 upon UV/VUV/CL excitation

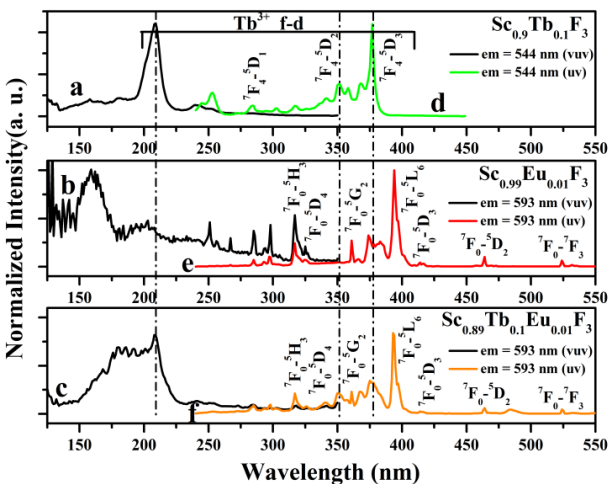

Fig. 6 Normalized excitation spectra of phosphors of $Sc_{0.9}Tb_{0.1}F_3$, $Sc_{0.99}Eu_{0.01}F_3$ and $Sc_{0.89}Tb_{0.1}Eu_{0.01}F_3$ in VUV (a, b, c)/UV (d, e, f) range

The primary object of this section is to the investigation of the luminescence properties of Tb^{3+}/Eu^{3+} doped ScF_3 and the sensitization effect in phosphors $Sc_{0.9-x}Eu_xTb_{0.1}F_3$. The excitation spectra of sample $Sc_{0.89}Tb_{0.1}Eu_{0.01}F_3$ in VUV-UV range are measured and compared with those of $Sc_{0.9}Tb_{0.1}F_3$ and $Sc_{0.99}Eu_{0.01}F_3$. These spectra are exhibited in Fig. 6. For clarity, each curve is normalized to its highest intensity. Under monitoring at 544 nm ($^5D_4$-$^7F_5$ transition of Tb^{3+}), the VUV excitation spectra a-c are all composed of a broad band with a maximum at ~165 nm due to the host absorption. Meanwhile, the strong band around 210 nm in curve a and c is correspond to the spin-allowed $4f^8 \rightarrow 4f^75d^1$ transition of Tb^{3+}, which is absent in curve b. And the sharp peaks in the spectral ranged from 300−500 nm in curve d (λ_{em} = 544 nm) and f (λ_{em} = 593 nm) are assigned to the intra configuration transitions f→ f transition of Tb^{3+} and Eu^{3+}, respectively[49, 50]. By monitoring at 593 nm ($^5D_0$-$^7F_1$ transition of Eu^{3+}), the excitation spectrum f of $Sc_{0.89}Eu_{0.01}Tb_{0.1}F_3$ also shows the $4f^8 \rightarrow 4f^75d^1$ transition of Tb^{3+}, i.e. the PLE spectrum of Tb^{3+} contribute to the PL spectrum of Eu^{3+}. Therefore, the ET from Tb^{3+} to Eu^{3+} exists possibly upon VUV and UV excitation.

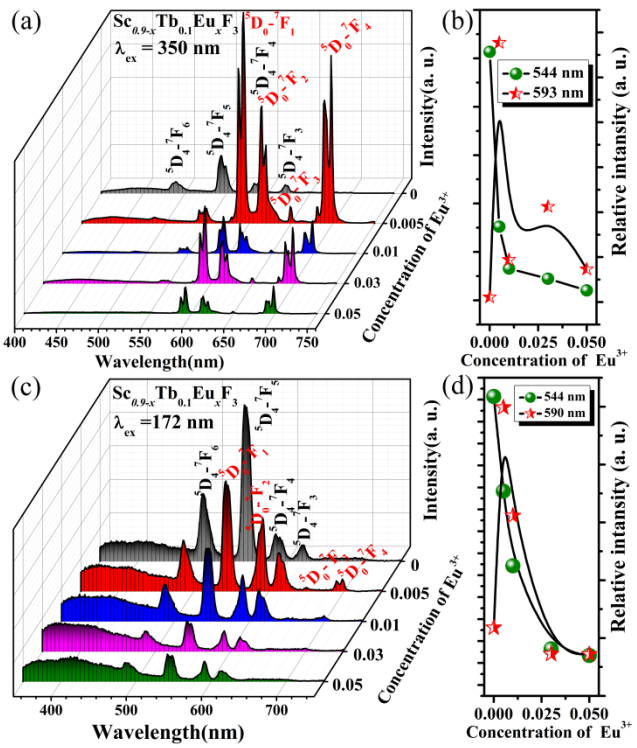

Fig. 7 Emission spectra (a, c) of $Sc_{0.9-x}Eu_xTb_{0.1}F_3$ ($0 \le x \le 0.05$) samples and the intensities of peak 544 nm and 593 nm of $Sc_{0.9-x}Eu_xTb_{0.1}F_3$ ($0 \le x \le 0.05$) as a function of concentration of Eu^{3+} under 350 nm (b) and 172nm excitation (d), respectively

Fig. 7a shows the emission spectra of $Sc_{0.9-x}Eu_xTb_{0.1}F_3$ ($0 \le x \le 0.05$) under 350 nm excitation corresponding to $^7F_4$-$^5D_2$ transition of Tb^{3+}. It is noted that all the spectra contain a broad band emission from 400 to 460 nm most likely arised from nanocrystal defects. In the formation process of the ScF_3 nanocrystals, the adsorbed CTAB molecules can introduce some oxygen and negative charges onto the surfaces of the ScF_3, and these will cause defects or electronic centers in the ScF_3 which can result in some trap states, similar phenomenon is also reported in other references[51-55]. And the broad feature of the trap state emission band indicates that there is a large number of trap states in the ScF_3. The excitation and emission spectra of ScF_3 nanocrystals under 350 and 172 nm excitation are exhibits in Fig. S1 and Fig. S2 in the ESI.†, respectively. In Tb^{3+} single doped ScF_3 sample, the sharp peaks in the range of 480-650 nm are assigned to $^5D_4$-^7F_J (J = 3, 4, 5, 6) transitions of Tb^{3+}. However, the transitions of $^5D_3$-^7F_J are not observed, which should have appeared in the range of 400-460 nm. The main reason lies to the concentration quenching by a cross-relaxation process ($^5D_3 + {}^7F_6 \rightarrow {}^5D_4 + {}^7F_0$) between two interacting Tb^{3+} centers. With the introduction of Eu^{3+}, besides Tb^{3+} emissions, the characteristic emissions of Eu^{3+} corresponding to $^5D_0$-$^7F_1$, 2, 3, 4 transitions can also be observed. Meanwhile, with increasing the Eu^{3+} concentration, the emission intensities of Tb^{3+} remarkably decrease but emission intensities of Eu^{3+} increases regularly, which is clearly illustrated in Fig. 7b, which further prove the efficient ET between Tb^{3+} and Eu^{3+} occurs. When Eu^{3+} concentration is higher than 0.005, the emission intensity decreases due to concentration quenching phenomenon. Under 172 nm excitation, these phosphors exhibit similar luminescence behaviors. The phenomenon could be expounded as follows.

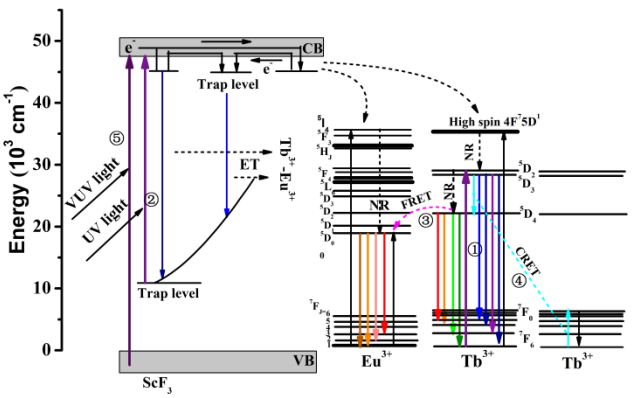

Fig. 8 A scheme showing the PL under UV/VUV excitation processes (FRET = fluorescence resonance energy transfer, NR = non-radiative transition, CRET = cross-relaxation energy transfer)

According to above data, the ET process could be described by the energy level scheme shown in Fig. 8. Under 350 nm excitation, the electrons of Tb^{3+} are excited to the $^5D_2$ level (process 1), and then the excited Tb^{3+} have two ways to get back to the ground state. One is a radiative transition from the 5d level to the 4f level. The other can transfer energy to nearby Eu^{3+} (process 3), cause Eu^{3+} emissions in the PL spectrum. The ratio of the Tb^{3+} and Eu^{3+} emission intensities mainly depends on the FRET efficiency from Tb^{3+} to Eu^{3+} [16, 17, 56]. And the cross-relaxation energy transfer (CRET) of Tb^{3+}-Tb^{3+} is exist (process 4). Meanwhile, the energy of 350 nm photon can excite the electrons on certain trap levels to conduction band (CB) (process 2). Generally speaking, the electrons in CB can move freely. Thus the activated electrons go on moving to other high trap level and then transit to the low trap states, which results in a broad band emission of defects. Because of the overlap of the emission

spectrum of defects and the excitation spectra of Tb^{3+} and Eu^{3+}, the ET of defects to Tb^{3+} and Eu^{3+} can also exist, which could enhance their luminescence. Dissimilarly, under 172 nm excitation, the energy is high enough to directly activate the electrons from (valence band) VB to CB (process 5). Subsequently, the free electrons partially transit to the high trap level. This part of electrons has two kinds of transition paths. On one hand, excited electrons transit from the valence band to the lower trap level, resulting in a broader emission than that under 350 nm excitation. On the other hand, high trap level electrons together with CB electrons can transfer energy to the upper states of Tb^{3+} and Eu^{3+}, resulting in the characteristic emission of Tb^{3+} and Eu^{3+} subsequently. Unsuspecting, the defects luminescence can also transfer energy to Tb^{3+} and Eu^{3+}. In addition to these, the FRET of Tb^{3+}-Eu^{3+} and CRET of Tb^{3+}-Tb^{3+} are both exist. It is noteworthy that the emissions of Eu^{3+} under 350 nm excitation (Fig. 7a) are much higher than that under 172 nm excitation (Fig. 7c). This phenomenon can be explained in this way: more additional defects can be produced due to the high energy of VUV photon, which will be impeditive to the ET, including the ET of host-Eu^{3+} and Tb^{3+}-Eu^{3+}, resulting in a weaker Eu^{3+} emission compared with that under 350 nm excitation. Just at this time, the reason why the emissions of Tb^{3+} is wearing off while increasing the content of Eu^{3+} under 172 nm excitation is mainly focused on two aspects, which are different from that under 350 nm excitation, too. One is that the concentration of Tb^{3+} is constant but the energy absorbed by Tb^{3+} and Eu^{3+} is competitive. Thus, more Eu^{3+} are introduced, less energy obtained by Tb^{3+} weakens the emission of Tb^{3+}. The other one is the ET between Tb^{3+} and Eu^{3+}. Therefore, $Sc_{0.9-x}Eu_xTb_{0.1}F_3$ phosphors exhibit various emissions under UV and VUV light and the emission color is tunable in a large color gamut, inferring that this series of phosphors is expected to have potential applications in LEDs, 3D PDPs and Hg-free lamps.

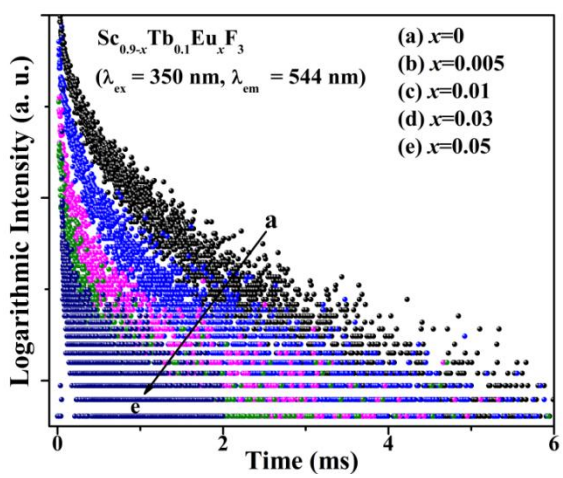

Fig. 9. Luminescence decays of Tb^{3+} in samples $Sc_{0.9-x}Tb_{0.1}Eu_xF_3$ ($0 \le x \le 0.05$; λ_{ex} = 350 nm, λ_{em} = 544 nm).

To further understand the ET process from Tb^{3+} to Eu^{3+} in $Sc_{0.9-x}Tb_{0.1}Eu_xF_3$ ($0 \le x \le 0.05$) phosphors, the PL decay curves of the Tb^{3+} (λ_{ex} = 350 nm, λ_{em} = 544 nm) are carried out and shown in Fig. 9. A near single-exponential decay process is observed with different Eu^{3+} contents. Additionally, a small deviation from exponential decay also occurs in $Sc_{0.9}Tb_{0.1}F_3$. For curve a, the deviation may result from such factors as the CRET between Tb^{3+} and Tb^{3+} and nanocrystal defects. From curve a to curve e, the Tb^{3+} decay becomes faster as the Eu^{3+} concentration increases; the corresponding fluorescence lifetimes are calculated and shown in Table 1. This phenomenon indicates that much more efficient ET from Tb^{3+} to Eu^{3+} occurs in high Eu^{3+} content samples. A simple experimental formula can be used to estimate the $Tb^{3+} \rightarrow Eu^{3+}$ ET probability ($P_{Tb\rightarrow Eu}$)[57].

$$P_{Tb\rightarrow Eu} = \left(\frac{1}{\tau}\right) - \left(\frac{1}{\tau_0}\right) \qquad (1)$$

Where τ_0 and τ are the Tb^{3+} donor lifetime in the absence and presence of Eu^{3+} acceptor, respectively. Furthermore, the ET efficiency ($\eta_{Tb\rightarrow Eu}$) is evaluated from eq 2[58].

$$\eta_{Tb\rightarrow Eu} = 1 - \left(\frac{\tau}{\tau_0}\right) \qquad (2)$$

According to the above formulas 1 and 2, the values of $P_{Tb\rightarrow Eu}$ and $\eta_{Tb\rightarrow Eu}$ can be calculated and also shown in Table 1, respectively. The results indicate that with increasing Eu^{3+} concentration gradually, the ET from Tb^{3+} to Eu^{3+} becomes more efficient and the highest ET efficiency is 69.2 %.

Table 1 The lifetime (τ), ET probability and ET efficiency of $Sc_{0.9-x}Tb_{0.1}Eu_xF_3$ ($0 \le x \le 0.05$) (λ_{ex} = 350 nm, λ_{em} =544 nm)

$Sc_{0.9-x}Tb_{0.1}Eu_xF_3$	Lifetime (ms)	ET probability	Energy transfer efficiency (%)
x = 0	5.2	0	0
x =0.005	4.9	0.01	5.8
x =0.01	3.4	0.10	34.6
x = 0.03	2.6	0.19	50.0
x = 0.05	1.6	0.43	69.2

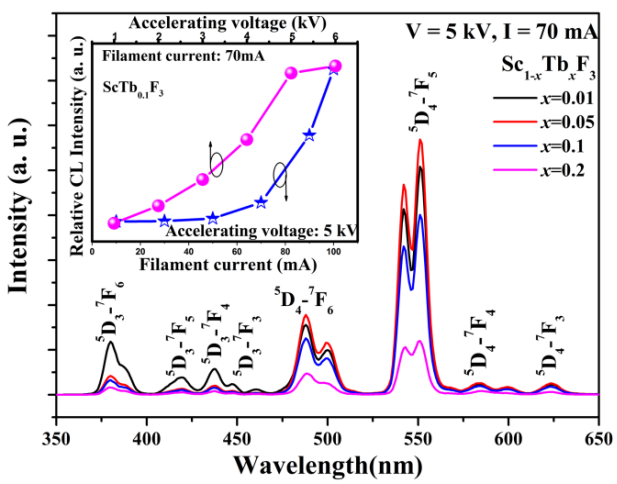

Fig. 10 CL spectra of $Sc_{1-x}Tb_xF_3$ ($0.01 \le x \le 0.2$), the insets show CL intensities of $0.1Tb^{3+}$ activated ScF_3 sample as a function of accelerating voltage and filament current.

To explore the potential application of the as-prepared ScF_3: Tb^{3+} phosphors in FED, their CL properties are investigated in detail. Under low-voltage electron-beam excitation (accelerating voltage = 5 kV, filament current = 70 mA), the CL spectra of ScF_3: xTb^{3+} ($0.01 \le x \le 0.2$) samples give the characteristic transitions of Tb^{3+} respectively, as shown in Fig. 10. Note that with the increasing of

Tb^{3+}, the transition of $^5D_3$-^7F_J of Tb^{3+} obviously quenched, indicating the cross-relaxation process ($^5D_3$ + $^7F_6$→ $^5D_4$ + $^7F_0$) between two interacting Tb^{3+} centers still exist in CL. Simultaneously, the transition of $^5D_4$-^7F_J of Tb^{3+} gradually enhance till the content of Tb^{3+} reaches to 5mol% due to concentration quenching phenomenon. Meanwhile the CL spectra of nanocrystal defects also exist as shown in Fig. S3 in the ESI.†. As is well known that the low-voltage CL properties of materials are important for FEDs, which are promising emissive displays realizing high resolution and low consumption of electronic power. So the CL emission intensities of $Sc_{0.95}Tb_{0.05}F_3$ samples have been further investigated as a function of the accelerating voltage and the filament current, as shown in the insets of Fig. 11. As the anode voltage increases, the penetrations of electron beam into phosphor layers increase too, so more activator ions are excited. Hence, an increase in CL intensity with increasing applied voltage occurs. When the filament current is fixed at 70 mA, the CL intensity increases as the accelerating voltage rises from 1 to 6 kV. Similarly, under the accelerating voltage = 5 kV electron beam excitation, the CL intensity also increases with increasing the filament current from 10 to 100 mA. There is no obvious saturation effect for the CL intensity of these samples with the increase of current density and accelerating voltage, indicating that the $Sc_{0.95}Tb_{0.05}F_3$ are resistant to the current saturation and have good conductivity, which is important for FED application. It is well known that when voltage increases, the carrier transport rate increases and current increases, the carrier concentration increases. The carrier transport rate or the carrier concentration increases, the higher is the conductivity, and the stronger is the emission. Accordingly, it is reasonable that there is no obvious saturation effect. The increase in CL brightness with an increase in electron energy and filament current is attributed to the deeper penetration of the electrons into the phosphor body and the larger electron-beam current density. The electron penetration depth under the different accelerating voltages are estimated in the ESI.†.

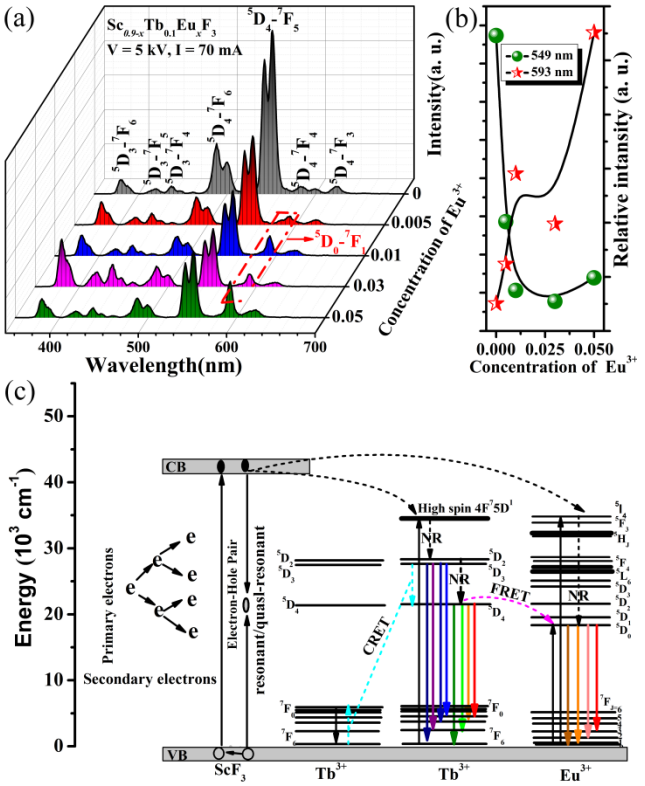

Fig. 11 CL spectra of $Sc_{0.9-x}Eu_xTb_{0.1}F_3$ ($0 \leq x \leq 0.05$) at the accelerating voltage of 5 kV and filament current of 70 mA (a); the intensities of peak 549 nm and593 nm as a function of concentration of Eu^{3+} (b); a scheme showing CL processes (c)

Systematically, the CL behavior of the Eu^{3+}, Tb^{3+} codoped ScF_3 phosphors under excitation of 5 kV and 70 mA are also studied and drawn in Fig. 11a. As compared to PL spectra, the CL spectra reveal almost similar behavior except the distinct and suprise appearance of $^5D_3$-^7F_J transitions of Tb^{3+}. This difference with PL can be attributed to their different luminescence mechanisms under the two excitation sources. The energy of UV/VUV photons used to excite luminescence materials is only around 3.1–12.4 eV. However, for CL, the energy of fast electrons under the accelerating anode voltage can be tuned from a few thousand to thousands of eV, leading to much larger excitation energy on a single particle in CL than in PL. On these grounds, possible luminescence mechanisms are proposed here concretely. For CL, the primary fast electrons create many secondary electrons. These secondary electrons excite the host lattice and create many electron–hole pairs, leading to the formation of bound excitons. These excitons decay nonradiatively through a resonant or quasi-resonant transfer to the upper states of Tb^{3+} and Eu^{3+} ions simultaneously, and give their characteristic emission. During this period, the FRET between Tb^{3+} and Eu^{3+} is also likely to happen. Though our experimental results, it is demonstrated that there are cross-relaxation process ($^5D_3$ + $^7F_6$→ $^5D_4$ + $^7F_0$) in $Sc_{0.9-x}Eu_xTb_{0.1}F_3$ under three kinds of excitation. It is different that both under excitations of UV and VUV photons, the cross-relaxation ET are efficient, in opposite, the cross-relaxation ET is relative low efficient excited by the fast electrons. Because for CL, there will create more defects than using UV/VUV as the exciting source since electrons obviously possess a lot more energy than photons. Now more defects may impede the cross-

relaxation ET process and the quenching of $^5D_3$-$^7F_6$ transition will be far from rapid, which results to an observable $^5D_3$-^7F_J emission of Tb^{3+}. And CL mechanism is intuitively illustrated in Fig. 11c. What's observed clearly from Fig. 11b is that with increasing Eu^{3+}, the $^5D_4$-^7F_J transitions of Tb^{3+} is wearing off and the characteristic transitions of Eu^{3+} are enhanced distinctly. Similarly, the phenomenon can root in the competing to absorb energy between Tb^{3+} and Eu^{3+} and ET of Tb^{3+}- Eu^{3+}. This is also responsible for the tunable color emission in the CL spectrum.

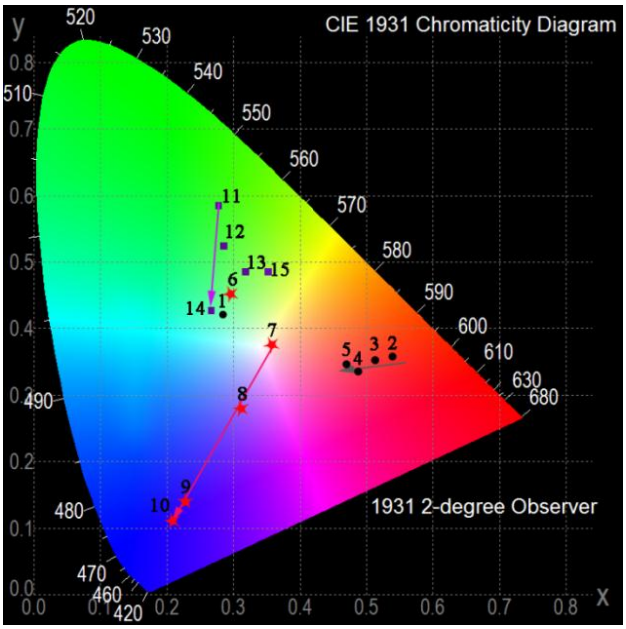

Fig. 12 CIE chromaticity diagram for $Sc_{0.9-x}Eu_xTb_{0.1}F_3$ ($0 \le x \le 0.05$) phosphors under different excitation sources (the black circle dots (1-5), red star dots (6-10) and purple square dots (11-15) represent the color coordinates of emissions under 350 nm, 172 nm and 5 kV and 70 mA excitation, respectively)

The CIE chromaticity coordinates for $Sc_{0.9-x}Eu_xTb_{0.1}F_3$ ($0 \le x \le 0.05$) phosphors under there different excitation sources are measured and drawn in Fig. 12 and Table 2, respectively. It is worth noting that there are there different color change rules under 350 nm, 172 nm and low-voltage electron-beam excitation, respectively. Under 350 nm excitation, with increasing Eu^{3+} content, the chromaticity coordinates vary systematically from (0.285, 0.409) to (0.474, 0.350), corresponding color tone of the $Sc_{0.9-x}Eu_xTb_{0.1}F_3$ samples shifts directly from green to red in the visible spectral region. The chromaticity coordinates of these phosphors upon 172 nm excitation primarily locate at (0.295, 0.460) and varies from (0.363, 0.384) to (0.208, 0.104) gradually, which clearly indicate that the color firstly be at yellow, then tunes from yellow to purple by controlling the Eu^{3+} concentration. Under low-voltage electron-beam excitation, almost all the color keep green and with increasing Eu^{3+} content, the chromaticity coordinates vary systematically from (0.277, 0.591) to (0.343, 0.496). In sum, the factors of the enhancement of the probability of ET along with the competition absorption between Tb^{3+} and Eu^{3+} and the broad luminescence of nanoparticle detects combine to bring about the multicolor emissions of $Sc_{0.9-x}Eu_xTb_{0.1}F_3$ phosphors.

Table 2 Comparison of CIE chromaticity coordinates for $Sc_{0.9-x}Eu_xTb_{0.1}F_3$ ($0 \le x \le 0.05$) under 350 nm, 172 nm and low-voltage electron-beam excitations

Sample	λ_{ex}=350 nm		λ_{ex}=172 nm		V=5kV, I=70mA	
	CIEx	CIEy	CIEx	CIEy	CIEx	CIEy
$Sc_{0.9}Tb_{0.1}F_3$	0.285	0.409	0.295	0.460	0.277	0.591
$Sc_{0.895}Eu_{0.005}Tb_{0.1}F_3$	0.534	0.363	0.363	0.384	0.281	0.530
$Sc_{0.89}Eu_{0.01}Tb_{0.1}F_3$	0.503	0.361	0.306	0.273	0.310	0.499
$Sc_{0.87}Eu_{0.03}Tb_{0.1}F_3$	0.495	0.333	0.230	0.149	0.272	0.413
$Sc_{0.85}Eu_{0.05}Tb_{0.1}F_3$	0.474	0.350	0.208	0.104	0.343	0.496

3.4.2 UC luminescence

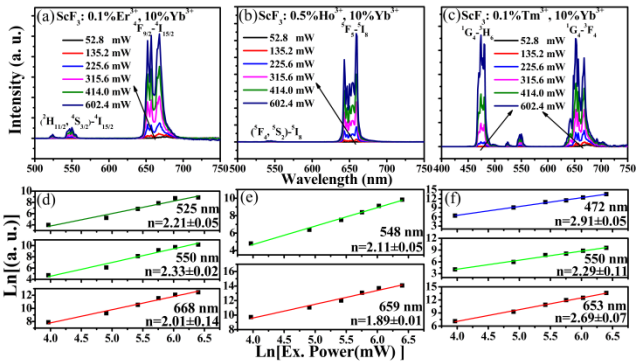

Fig. 13 UC spectra of (a) Yb^{3+}–Er^{3+} (b) Yb^{3+}–Tm^{3+} (c) Yb^{3+}–Ho^{3+} co-doped ScF_3 under different pump power densities and the plots of ln I versus P yields a straight line with slope n (d, e, f).

It is necessary to explore the UC luminescence properties of nanocrystals due to their numerous potential applications. Thus under 980 nm LD excitation at the different pump powers, the corresponding UC emission spectra of the as-prepared ScF_3: Yb^{3+}, Ln^{3+} (Ln = Er/Ho/Tm) are shown in Fig. 13a-c. For ScF_3: 0.1Yb^{3+}, 0.001Er^{3+}, the three emission peaks around 525, 550 and 668 nm in Fig. 13a could be attributed to the $^2H_{11/2}/^4I_{15/2}$, $^4S_{3/2}/^4I_{15/2}$ and $^4F_{9/2}/^4I_{15/2}$ transitions of Er^{3+}, respectively. To understand the mechanism of the UC process, we have performed power dependent studies. The laser power (P) is related to the number of photons involved in producing the UC emission via the equation $P \propto I^n$, where I is the intensity of the UC emission and n is the number of photons[59]. In terms of every emission peak at 525, 550 and 668 nm, a plot of ln I versus P yields a straight line with slope n as shown in Fig. 13d, and the results are n = 2.21, 2.33 and 2.01, respectively. This suggests it is a two-photon process. Synchronously, a near-infrared to near-infrared UC luminescence process is observed in Yb^{3+}-Ho^{3+} codoped ScF_3. The ScF_3: 0.1Yb^{3+}, 0.005Ho^{3+} sample exhibits a green emission at 548 nm and a strong red emission at 659 nm, resulting from the $^5S_2$–$^5I_8$ and $^5F_5$–$^5I_8$ transitions of Ho^{3+}, as shown in Fig. 13b. The calculated values of n are 2.11, 1.89 for the 548 and 659 nm emissions, respectively. Hence, the main UC mechanism for Yb^{3+}-Ho^{3+} pairs in this host is a two photon process. Fig. 13c displays an intense blue emission (472 nm), a weak green emission (550 nm) and an intense red emission (653 nm). These peaks are quite characteristic of Tm^{3+} and are assigned to the $^1G_4$–$^3H_6$, $^3F_{2,3}$-$^3H_6$ and $^1G_4$-$^3F_4$ transitions, respectively. From Fig. 13f, the calculated values of n are 2.91, 2.29 and 2.69 for the 472, 550 and 653 nm emissions, respectively. This implies that it is involved of 3, 2 and 3 photons of 980 nm in producing blue, green and red emissions. The several possible mechanism for

multi-photon process with energy level diagrams of Yb^{3+}–Er^{3+}, Yb^{3+}–Ho^{3+}, Yb^{3+}–Tm^{3+} co-doped ScF_3 under 980 nm laser diode excitation is discussed in detail, as shown in the ESI.†. It is very special revealed from Fig. 13f that the blue emission assigned to $^1G_4$–$^3H_6$ transition of Tm^{3+} enhances with pump power densities more fast than that of $^1G_4$-$^3F_4$ transition of Tm^{3+}. In this case, the blue emission process of Tm^{3+} is more sensitive to the change of pump power according to the above computation.

3.5 Magnetism properties

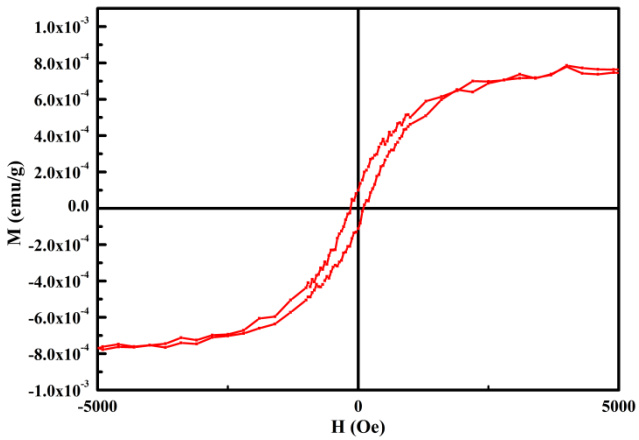

Fig. 14.Magnetization *vs.* magnetic field of ScF_3 nanocrystals.

For the luminescence materials applied in magnetic resonance imaging, bioprocess and drug delivery, magnetism is of great concern[60, 61]. The magnetization versus magnetic field (M-H) curves for the ScF_3 nanocrystals recorded at RT are shown in Fig. 14 It can be seen that the measured coercivities and the saturated magnetizations (Ms) of the ScF_3 nanocrystals are 158 Oe, 7.75×10^{-4} emu/g. According to the principle, the unpaired electrons show the abnormal spin phenomenon, which can cause the magnetism. We suggest the unpaired electrons originated from the defects on the surfaces of the nanoparticles are responsible for the ferromagnetism in ScF_3 nanocrystals[62-64]. In contrast to the iron oxides, the Ln^{3+} ions doped ScF_3 nanocrystal exhibits both intrinsic luminescence and magnetism properties, indicating its potential applications in bioseparation and magnetic resonance imaging.

4. Conclusion

In summary, multifunctional ScF_3: Ln^{3+} (Ln = Tb, Eu, Yb, Er, Tm and Ho) nanocrystals have been successfully synthesized via hydrothermal/solvothermal synthesis process. The morphology, electronic structure, magnetism and tunable luminescence properties of the as-obtained samples are all characterized. ScF_3 own the indirect band gap of 6.075 eV, hinting its potential good properties as the matrix. Most interesting, it is found that under UV, VUV and low-voltage electron beam excitation, the as-obtained Tb^{3+}, Eu^{3+} codoped ScF_3 product exhibit multicolor emissions together with probable ET process, competition of energy absorption and broad luminescence of nanocrystal defects. Correspondingly, the different luminescence mechanisms are proposed. Furthermore, Yb^{3+}, Tm^{3+}/Er^{3+}/Ho^{3+} codoped ScF_3 show good UC luminescence properties. The real agreeable is that ScF_3 nanocrystals exhibit ferromagnetism at RT. All of these nice properties can find potential applications of these phosphors in PL areas, field emission display devices and bioseparation and magnetic resonance imaging and so forth.

Acknowledgements

This work is supported by National Science Foundation for Distinguished Young Scholars (No. 50925206), Specialized Research Fund for the Doctoral Program of Higher Education (No. 20120211130003), the National Natural Science Funds of China (Grant No. 51372105).

Notes and references

[a]*Department of Material Science, School of Physical Science and Technology, Lanzhou University, Lanzhou 730000, China*
[b]*Laboratory of Beijing Synchrotron Radiation, Institute of High Energy Physics, Chinese Academy of Sciences, Beijing 100049, China*
† *Electronic Supplementary Information (ESI) available: [The UV/VUV/CL spectra of nanocrystal defects in ScF_3 and the calculation of electron penetration depths]. See DOI: 10.1039/b000000x/*

1 A. Birkel, K. A. Denault, N. C. George, C. E. Doll, B. Héry, A. A. Mikhailovsky, C. S. Birkel, B. C. Hong and R. Seshadri, *Chem. Mater.*, 2012, **24**, 1198.
2 X. L. Liu, Y. X. Liu, D. T. Yan, H. C. Zhu, C. G. Liu, C. S. Xu, Y. C. Liu and X. J. Wang, *J. Mater. Chem.*, 2012, **22**, 16839.
3 D. Y. Wang, Y. C. Chen, C. H. Huang, B. M. Cheng and T. M. Chen, *J. Mater. Chem.*, 2012, **22**, 9957.
4 B. L. Abrams and P. H. Holloway, Chem. Rev., 2004, 104, 5783.
5 X. Y. Yang, J. Liu, H. Yang, X. B. Yu, Y. Z. Guo, Y. Q. Zhou and J. Y. Liu, *J. Mater. Chem.*, 2009, **19**, 3771.
6 Y. F. Wang, X. Xu, L. J. Yin and L. Y. Hao, *Electrochem. Solid State Lett.*, 2010, **13**, 119.
7 Z. F. Tian, H. B. Liang, W. P. Chen, Q. Su, G. B. Zhang and G. T. Yang, *Opt. Express*, 2009, **17**, 956.
8 K. Y. Jung, H. W. Lee, Y. C. Kang, S. B. Park and Y. S. Yang, *Chem. Mater.*, **2005, *17***, 2729.
9 J. D. Ghys, R. Mauricot, B. Caillier, P. Guillot, T. Beaudette, G. H. Jia, P. A. Tanner and B. M. Cheng, *J. Phys. Chem. C*, 2010, **114**, 6681.
10 F. L. Zhang, S. Yang, C. Stoffers, J. Penczek, P. N. Yocom, D. Zaremba, B. K. Wagner and C. J. Summers, *Appl. Phys. Lett.*, 1998, **72**, 2226.
11 Y. C. Li, Y. H. Chang, Y. F. Lin, Y. J. Lin and Y. S. Chang, *Appl. Phys. Lett.*, 2006, **89**, 081110.
12 M. Shang, G. Li, D. Yang, X. Kang, C. Zhang and J. Lin, *J. Electrochem. Soc.*, 2011, **158**, 125.
13 N. Guo, H. P. You, Y. H. Song, M. Yang, K. Liu, Y. H. Zheng, Y. J. Huang and H. J. Zhang, *J. Mater. Chem.*, 2010, **20**, 9061.
14 G. G. Li, Y. Zhang, D. L. Geng, M. M. Shang, C. Peng, Z. Y. Cheng and J. Lin, *ACS Appl. Mater. Interfaces*, 2011, **4**, 296.
15 R. S. Liu, Y. H. Liu, N. C. Bagkar and S. F. Hu, Appl. Phys. Lett., 2007, **91**, 061119.
16 S. H. Park, S. I. Mho, C. H. Kim, B. S. Jeong and H. L. Park, *Solid State Commun.*, 1992, **83**, 47.
17 J. Huan, W. Jiaguo, L. Fuhui, T. Shujian and J. Xiping, *J. Electrochem. Soc.*, 2004, **151**, H49.
18 V. B. Mikhailik, H. Kraus and P. Dorenbos, *Phys. Status Solidi RRL*, 2009, **3**, 13.
19 V. B. Mikhailik and H. J. Kraus, *Lumin.*, 2009, **129**, 945.
20 V. B. Mikhailik and H. Kraus, *Phys. Status Solidi A*, 2010, **207**, 2339.
21 Z. L.Wang, H. L. W. Chan, H. L. Li and J. H. Hao, *Appl. Phys. Lett.*, 2008, **93**, 141106.
22 P. Rahman and M. Green, *Nanoscale*, 2009, **1**, 214.
23 M. Haase and H. Schaefer, *Angew. Chem., Int. Ed.*, 2011, **50**, 5808.
24 N. M. Shavaleev, F. Gumy, R. Scopelliti and J.-C. G. Bünzli, *Inorg. Chem.*, 2009, **48**, 5611.
25 K. Blomberg, P. Hurskainen and I. Hemmila, *Clin. Chem.*, 1999, **45**, 855.

26 Y. Dai, P. A. Ma, Z. Cheng, X. Kang, X. Zhang, Z. Hou, C. Li, D. Yang, X. Zhai and J. Lin, *ACS Nano*, 2012, **6**, 3327.
27 B. Zhou, L. L. Tao, Y. H. Tsang and We. Jin, *J. Mater. Chem. C*, 2013, **1**,4313
28 J. Wang, F. Wang, C. Wang, Z. Liu, and X. G. Liu, *Angew. Chem. Int. Ed*. 2011, **50**, 10369
29 W. Song, A. E. Vasdekis, Z. Li and D. Psaltis, *Appl. Phys. Lett.*, 2009, **94**, 051117.
30 Y. Li, J. Zhang, Y. Luo, X. Zhang, Z. Hao and X. Wang, *J. Mater. Chem.*, 2011, **21**, 2895.
31 J. H. Chuang, J. H. Ryu, S. W. Mhin, K. M. Kim and K. B. Shim, *J. Mater. Chem.*, 2012, **22**, 3997
32 Y. S. Liu, D. T. Tu, H. M. Zhu, E. Ma and X. Y. Chen, *Nanoscale*, 2013, **5**, 1369.
33 F. C. J. M. van Veggel, C. H. Dong, N. J. J. Johnson and J. Pichaandi, *Nanoscale*, 2012, **4**, 7309.
34 J. L. Adam, *Chem. Rev.*, 2002, **102**, 2461.
35 J. W. Stouwdam, G. A. Hebbink, J. Huskens, F. C. J. M. van Veggel, *Chem. Mater.* 2003, **15**, 4604.
36 K. S. Aleksandrov, V. N. Voronov and A. N. Vtyurin, S. V. Goryainov, N. G. Zamkova, V. I. Zinenko and A. S. Krylov, *J. Exp. Theor. Phys.*, 2002, **94**, 977.
37 O. Greis, R. Ziel, H.-j. Klammer, C. Sassin, A. Haase, B. P. Breidenstein, *Private Comm.*, 1995.
38 B. K. Greve, K. L. Martin, P. L. Lee, P. J. Chupas, K. W. Chapman and A. P. Wilkinson, *J. Am. Chem. Soc.*, 2010, **132**, 15496.
39 L. Zhang, Y. S. Wang, Y. Yang, F. Zhang, W. F. Dong, S. Y. Zhou, W. H. Pei, H. D. Chen and H. B. Sun, *Chem. Commun.*, 2012, 48, 11238.
40 X. B. Li, S. L. Gai, C. X. Li, D. Wang, N. Niu, F. He and P. P. Yang, *Inorg. Chem.*, 2012, 51, 3963.
41 J. Yang, C. X. Li, X. M. Zhang, Z. W. Quan, C. M. Zhang, H. Y. Li and J. Lin, *Chem. Eur. J*, 2008, **14**, 4336.
42 R. F. Qin, H. W. Song, G. H. Pan, X. Bai, B. Dong, S. H. Xie, L. N. Liu, Q. L. Dai, X. S. Qu, X. G. Ren and H. F. Zhao, *Cryst. Growth Des.*, 2009, **9**, 1750.
43 I. F. Li, C. H. Su, H. S. Sheu, H. C. Chiu, Y. W. Lo, W. T. Lin, J. H. Chen and C. S. Yeh, *Adv. Funct. Mater.*, 2008, **18**, 766
44 H. F. Liu, S. F. Ji, Y. Y. Zheng, M. Li and H. Yang, *Powder Technol.*, 2013, **246**, 520
45 Z. H. Xu, X. J. Kang, C. X. Li, Z. Y. Hou, C. M. Zhang, D. M. Yang, G. G. Li and J. Lin, *Inorg. Chem.*, 2010, **49**, 6706.
46 T. X. Wang, H. Colfen and M. Antonietti, *J. Am. Chem. Soc.*, 2005, **127**, 3246.
47 C. X. Li, J. Yang, P. P. Yang, H. Z. Lian and J. Lin, *Chem. Mater.*, 2008, **20**, 4317.
48 Y. Tian, B. J. Chen, X. P. Li, J. S. Zhang, B. N. Tian, J. S. Sun, L. H. Cheng, H. Y. Zhong, H. Zhong, R. N. Hua, *J. Solid State Chem.*, 2012, **196**, 187.
49 Y. G. Su, L. P. Li and G. S. Li, *Chem. Mater.*, 2008, **20**, 6060.
50 Y. Tian, X. H. Qi, X. W. Wu, R. N. Hua and B. J. Chen, *J. Phys. Chem. C*, 2009, **113**, 10767.
51 W. H. Green, K. P. Le, J. Grey, T. T. Au and M. J. Sailor, *Science*, 1997, **276**, 1826.
52 J. Joo, H. B. Na, T. Yu, J. H. Yu, Y. W. Kim, F. X. Wu, J. Z. Zhang and T. Hyeon, *J. Am. Chem. Soc.*, 2003, **125**, 11100.
53 X. M. Zhang, Z. W. Quan, J. Yang, P. P. Yang, H. Z. Lian and J. Lin, *Nanotechnology*, 2008, **19**, 075603.
54 C. K. Lin, M. Yu, Z. Y. Cheng, C. M. Zhang, Q. G. Meng and J. Lin, *Inorg. Chem.*, 2008, **47**, 49.
55 C. M. Zhang, C. K. Lin, C. X. Li, Z. W. Quan, X. M. Liu and J. Lin, *J. Phys. Chem. C*, 2008, **112**, 2183.
56 X. L. Liang, Z. Y. Lin, Y. X. Yang, Z. W. Xing and G. R. Chen, *J. Am. Ceram. Soc.*, 2012, **95**, 275
57 D. Ananias, M. Kostova, F. A. A. Paz, A. Ferreira, L. D. Carlos, J. Klinowski and J. Rocha, *J. Am. Chem. Soc.*, 2004, **126**, 10410.
58 Z. D. Hao, J. H. Zhang, X. Zhang, S. Z. Lu and X. J. Wang, *J. Electrochem. Soc.* 2009, **156**, 193.
59 M. Pollnau, D. R. Gamelin, S. R. Luthi, H. U. Güdel and M. P. Hehlen, *Phys. Rev. B*, 2000, **61**, 3337.
60 B. Ankamwar, T. C. Lai, J. H. Huang, R. S. Liu, M. Hsiao, C. H. Chen and Y. K. Hwu, *Nanotechnology*, 2010, **21**, 075102.
61 S. Shylesh, V. Schunemann and W.R. Thiel, *Angew. Chem. Int. Edit.*, 2010, **49**, 3428.
62 H. Ohno, A. Shen, F. Matsukura, A. Oiwa, A. Endo, S. Katsumoto, and Y. Iye, *Appl. Phys. Lett.*, 1996, **69**, 15.
63 D. Q. Gao, J. Zhang, J. Y. Zhu, J. Qi, Z. H. Zhang, W. B. Sui, H. G. Shi and D. S. Xue, *Nanoscale Res. Lett.*, 2010, **5**, 769.
64 D. Q. Gao, Z. H. Zhang, J. L. Fu, Y. Xu, J. Qi, and D. S. Xue, *J. Appl. Phys.*, 2009, **105**, 113928.